Research paper

Experimental measurement of the bearing characteristics of straight-line flexure mechanisms

Shorya Awtar *, Dhanushkodi D. Mariappan

Precision Systems Design Lab, Mechanical Engineering, University of Michigan, 2350 Hayward Street, Ann Arbor, MI 48109, United States

A R T I C L E   I N F O

A B S T R A C T

In this paper, we present an experimental set-up and procedure to accurately measure the bearing characteristics of any single Degree of Freedom (DoF) straight-line flexure mechanism. Bearing characteristics include stiffness in the bearing and motion directions, and error motions in the bearing directions. In particular, we present this characterization for the traditional paired double parallelogram (DP-DP) flexure and its recently-reported improved variation, the clamped paired double parallelogram (C-DP-DP) flexure. Of particular interest is the bearing direction stiffness and its variation with motion direction displacement. While the bearing stiffness for both mechanisms has been extensively predicted via analysis and its consequences have been observed in experiments, its direct measurement poses several challenges and is not found in the literature. This paper presents an experimental set-up that is reconfigurable to accommodate both the above two flexures, comprises a novel virtual pulley concept, and employs carefully selected ground mounting and sensor locations, among other features that enable the desired measurements. The experimental results agree well with analytical predictions and generate insight into the importance of ground mounting, finite compliance of mechanism features that are generally assumed to be rigid, and manufacturing tolerances.

© 2017 Elsevier Inc. All rights reserved.

1. Introduction and background

Flexures are machine elements that provide motion via elastic deformation. Multiple flexure elements such as the beam flexure are combined to form a flexure mechanism that provides motion guidance and load bearing [1–4]. Owing to their joint-less construction, flexure mechanisms operate without friction, backlash, and wear, resulting in high motion precision (or repeatability) and zero maintenance. They also offer design simplicity due to minimal or no assembly, and therefore are highly suitable for monolithic micro-fabricated devices. Because of these various attributes, flexure mechanisms are used in high precision motion stages, MEMS devices, and harsh environments in wide range of applications [1–4].

Similar to a rigid-link mechanism, a flexure mechanism has certain motion directions (also known as degrees of freedom or DoF) and complementary bearing directions (also known as degrees of constraint or DoC). In this paper, we consider flexure mechanisms that provide a single translational DoF, with approximately straight-line motion. A classic example of a planar single translational DoF design is the double parallelogram (DP) flexure and

its symmetric paired version DP-DP flexure (shown in Fig. 1a). A planar design is one that is based on a two-dimensional geometry implemented on a flat plate material. Common examples include MEMS devices that are fabricated on silicon wafers via photolithography, and macro scale devices fabricated on metal plates using wire electric discharge machining (EDM) or water-jet cutting. Typically, the thickness of the flat plate is chosen to be large to provide high stiffness in the three out-of-plane directions, which can therefore be treated as DoC. While the stiffness characteristics in these out-of-plane directions are important and warrant analytical and experimental investigation [5,6], this paper focusses on the characterization of the in-plane DoF and DoC directions shown in Fig. 1a.

The symmetrically paired DP-DP flexure offers good overall bearing characteristics in terms of large range and low stiffness in the DoF direction, and theoretically zero error motions in DoC direction [1–4]. However, the main limitation of this design is that even though it provides a high bearing stiffness K_x when Y displacement is zero, this bearing stiffness drops precipitously at increasing values of Y displacement. This is due to the fact that the secondary stage in the DP flexure module is kinematically under-constrained, a phenomenon that has been extensively reported qualitatively and analytically in the past [1,2,7,8]. This bearing stiffness drop in the DP and DP-DP flexures with increasing Y displacement results in compromised performance in various applications. For example, it

* Corresponding author.
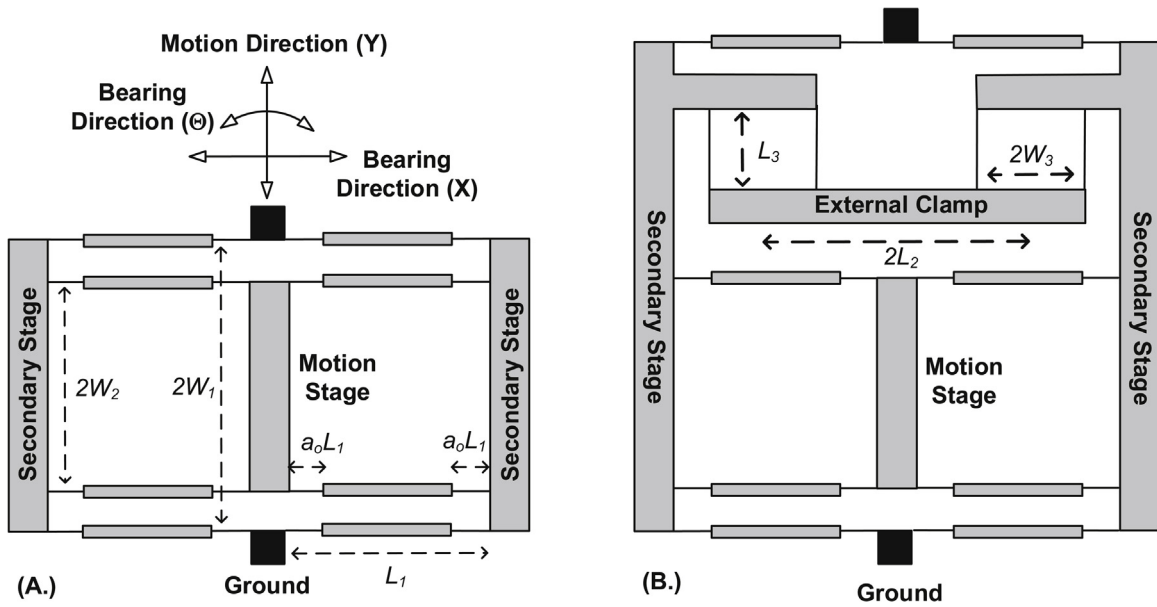   *E-mail address:* awtar@umich.edu (S. Awtar).

Fig. 1. (a) DP-DP Flexure (b) C-DP-DP Flexure.

leads to limited stroke in electrostatic comb-drive actuators [9,10] and moving magnet actuators [11] due to sideways snap-in.

In the past, the problem of under-constraint in the DP flexure geometry has been overcome via the use of a lever arrangement to enforce a 1:2 displacement ratio between the secondary stage and motion stage [7]. A monolithic flexure-based version of this lever solution has also been successfully implemented [12,13]. More recently, this 1:2 lever solution has been implemented via a sub-mechanism cleverly nestled within the DP flexure [14], leading to a compact foot-print. An alternate approach to constrain the secondary stages in the DP-DP flexure has been to couple the two secondary stages via an external clamp that forces the two secondary stages to move together in the Y direction but still allows any relative X displacement [10]. This design, referred to as the Clamped Paired Double Parallelogram (C-DP-DP) flexure, is shown in Fig. 1b. In yet another configuration, an asymmetric combination of the DP flexure and the tilted-beam DP flexure has been used to kinematically constrain the Secondary Stage of the latter [15]. These designs indeed produce the desired improvement in the bearing direction stiffness, making the drop in bearing stiffness more gradual, as shown via analytical modeling or finite element analysis (FEA). However, to the best of our knowledge, explicit experimental measurements of the bearing stiffness (K_x and K_θ) and their variation over motion direction displacement, for any of these designs, has not been reported in the prior literature and is the primary objective of this paper. Additional objectives include measurement of the X and Θ direction error motions (E_x and E_θ, respectively) as well as the motion direction stiffness K_y. Here Θ direction refers to in-plane rotation about the Z axis. Specifically, we have conducted these measurements on the DP-DP and C-DP-DP flexures, to show the improved bearing stiffness characteristics of the latter.

Measurement of the bearing stiffness is challenging because it requires accurate and precise measurements of very small deflections in the bearing direction for different values of bearing force and motion direction displacement. For a typical desktop size set-up, these deflections can be in the range of hundreds of nanometers to a few microns. At this scale, several factors can adversely affect the measurements:

1. Unanticipated sources of compliance (or parasitic compliance) in the experimental set-up can contribute additional deflection

when a bearing force is applied. This includes the various stages in the flexure mechanism that are nominally assumed "rigid" but have finite compliance. The flexure mechanism's ground plate and mounting to the experiment table also have finite compliance.

2. The method used to apply the bearing direction load has to be such that it does not introduce any hysteresis, so as to ensure a high degree of repeatability in the small bearing direction displacement measurements. Providing such bearing direction actuation over a range of motion direction displacements makes the experimental set-up design challenging.

3. Motion direction actuation must be such that it only provides a motion direction force and does not lead to additional forces in the bearing direction due to the flexure mechanism's bearing direction error motions, if any. This additional bearing direction force will produce additional bearing direction displacement, which can corrupt the desired measurement.

4. Sensors for measuring the bearing direction displacement should have adequate range, resolution, and accuracy and minimal sensitivity to environmental disturbances (e.g. temperature fluctuation). Also, the sensor should ideally be non-contact to avoid any friction or hysteresis in the bearing direction. Furthermore, measurements can have drift due to environmental variations. The experimental setup and process has to be designed to filter out any such drift.

5. Sensor and actuator mountings have to be designed carefully to provide a secure assembly and at the same time avoid friction, backlash, and the effects of parasitic compliance.

The experimental set-up design presented in this paper (Fig. 2) overcomes all of the above challenges. The sources of error are either eliminated via appropriate design or are systematically identified and separated from the desired measurand. The primary contributions of this work are:

1. This paper presents the first direct measurement, to the authors best knowledge, of the bearing direction stiffness (K_x and K_θ) of single translational DoF flexure mechanisms (DP-DP and C-DP-DP) as a function of the motion direction displacement. These measurements agree well with FEA predictions.
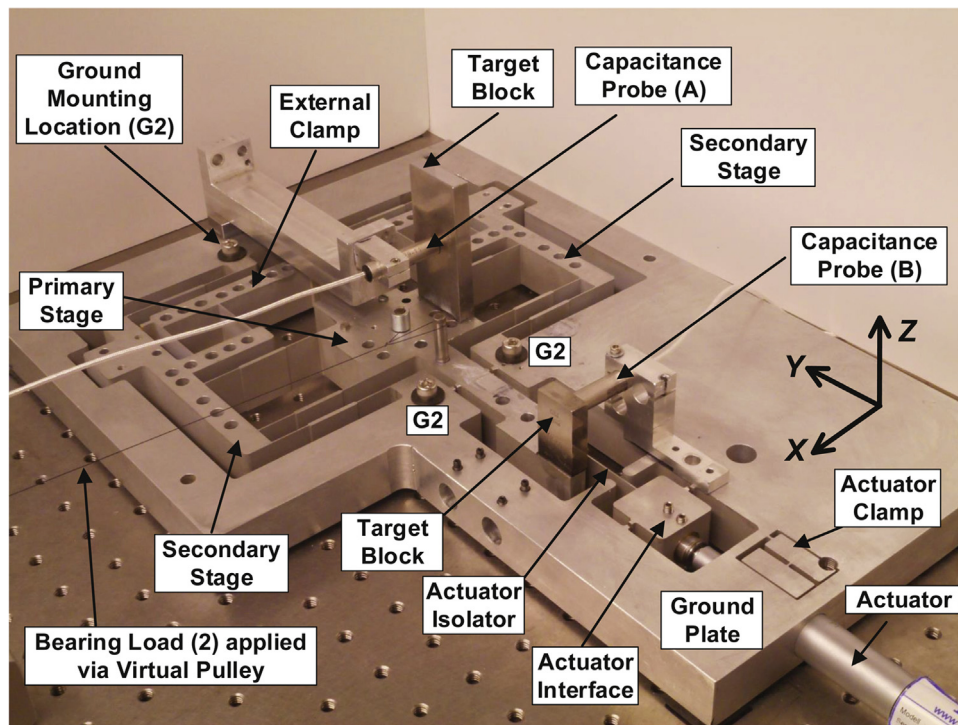
Fig. 2. Experimental Set-up for Bearing Stiffness Characterization.

2. This paper presents several innovations and careful design considerations in the experimental setup and procedure to enable the above measurements. This includes the application of the bearing direction force via a novel virtual pulley concept that completely eliminates friction and hysteresis, enabling precise measurements of small displacements. An actuator decoupler is incorporated in the motion direction actuation. Ground mounting locations between the experimental setup's ground plate and an optical table-top are strategically selected to minimize distortion of the ground plate due to its finite compliance. Sensors are chosen to provide non-contact measurement with high repeatability and accuracy; these sensors are located on the ground plate to minimize sensitivity to the ground plate's distortion, if any. The experimental set-up is designed to be highly modular such that both the DP-DP and C-DP-DP flexure measurements are accomplished via the same hardware. A systematic experimental procedure is developed to reject measurement drift. This basic set-up and the techniques for stiffness measurement are in general relevant and instructive for the experimental characterization of any flexure mechanism or structure.

3. This modeling and experimental work reveals several physical insights that can be potentially useful in flexure mechanism design. We highlight the significance of parasitic compliance associated with various stages, generally assumed rigid, and their impact on bearing stiffness. We also discuss the importance of selecting ground mounting locations and finite compliance of the ground plate/structure, and their impact on flexure bearing performance as well as experimental setup design (e.g. sensor and actuator mounting). We also demonstrate the impact of manufacturing tolerances and imperfections, which are inevitable, on flexure bearing performance.

Section 2 in this paper presents preliminary analysis to guide the design of the experimental setup and inform the choice of bearing dimensions, sensors, actuator and the loading configuration. Section 3 presents the detailed design of the experimental setup

including selection/fabrication and assembly of hardware components. Section 4 focusses on the experimental procedure used to conduct the experiments and acquire data, along with a discussion on how the raw data is processed. Section 5 presents a comparison between the experimental measurements and finite element analysis, along with a discussion on these results.

2. Preliminary analysis for the experimental setup design

2.1. Flexure bearing design and dimensions

The basic design of the flexure bearing used in this experimental set-up is shown in Fig. 3. Aluminum 6061-T651 (25.4 mm thick stock plate) was selected as the bearing material because of its ease of availability and machining, and dimensional stability over time [1]. This large out-of-plane (Z direction) dimension ensures that motions in the out-of-plane directions (i.e. displacement in Z, and rotations about X and Y) are much smaller than motions in the in-plane directions (i.e. displacements in X and Y, and rotation about Z), allowing the focus of this investigation to remain on the latter. The remaining dimensions for the flexure bearing were selected to achieve: (i) a reasonably sized benchtop experimental setup, (ii) motion direction displacement range that is at least 10% of the individual beam flexure length so as to reveal the non-linearities that give rise to bearing direction stiffness variation, and (iii) a margin of safety against static failure for this motion direction displacement range.

Furthermore, the flexure bearing was designed so that the same hardware set-up incorporates both the DP-DP and CDP-DP geometries. As shown in Fig. 3, the flexure bearing was initially fabricated in the C-DP-DP geometry. The secondary stages of the two DP flexures are connected to an external clamp via two parallelogram flexures. Once this geometry was experimentally tested and characterized, the beams of these two parallelogram flexure were simply cut off with a saw blade, thereby reducing the bearing to the DP-DP design. This was be followed by another round of experimental testing and characterization of the DP-DP design. Each of the
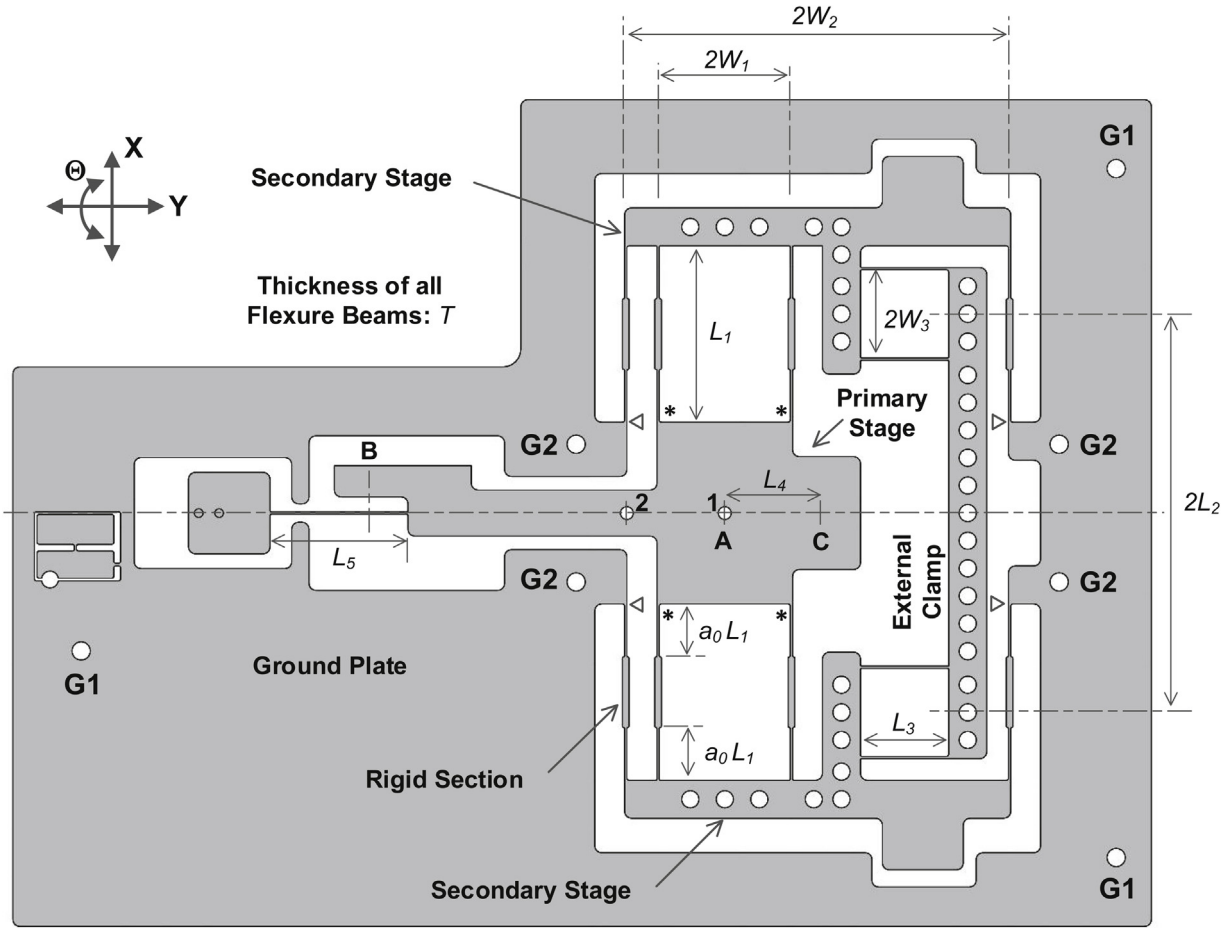
Fig. 3. CAD Model of the CDPDP Flexure Mechanism.

beams in the DP modules in the flexure bearing was designed with a rigid section in middle, which has shown to improve bearing direction stiffness without an adverse effect on the motion direction stiffness [2,3,8].

There exist extensive closed-form analyses for the DP-DP and C-DP-DP flexures that parametrically relate the mechanism dimensions to their stiffness properties [1,8,10]. However, all these past analyses have assumed symmetric DP-DP and C-DP-DP design, i.e. the centers of the inner and outer parallelograms in the DP modules with these flexure mechanisms were coincident. However, in the present case, the center of inner parallelogram along the Y axis (point "A" in Fig. 3) is not coincident with the center of the outer parallelogram (point "C" in Fig. 3) due to geometric layout reasons. Therefore, prior analytical expressions for stiffness in X, Θ (rotation about Z), and Y directions have been updated taking into account the distance L_4 between these two centers, and are presented below for both the DP-DP and C-DP-DP flexure mechanisms:

$$K_x = \frac{EI}{L_1^3} \frac{2k_{33}}{\left(\frac{Y}{L_1}\right)^2 2k_{33}\left(\left(1+\frac{L_4^2}{2W_1^2}\right)\frac{g_{11}^{(1)}}{8} + \frac{\left(k_{11}^{(1)}\right)^2}{4k_{11}^{(0)}(1+\eta)}\right) - \left(\frac{Y}{L_1}\right)\frac{L_4^2}{2W_1^2}\left(\frac{k_{12}^{(0)}k_{11}^{(1)}}{2k_{11}^{(0)}} - \frac{k_{12}^{(1)}}{2}\right) + \left(1+\frac{L_4^2}{2W_1^2}\right)} \tag{1}$$

$$K_\theta = \frac{EI}{L_1^3}\left(\frac{4W_1^2 W_2^2}{W_1^2 + W_2^2}\right)\frac{1}{\left(\frac{1}{k_{33}} + \frac{g_{11}^{(1)}}{4}\left(\frac{Y}{L_1}\right)^2\right)} \tag{2}$$

$$K_y = \frac{2EI}{L_1^3}\left(k_{11}^{(0)} + \lambda\left(\frac{Y}{L_1}\right)^2\right) \tag{3}$$

where, $\eta = \frac{6W_2^2 L_1^3}{k_{11}^{(0)}L_2^2 L_3 T^2}$ and $\lambda = \frac{9k_{11}^{(0)}k_{11}^{(1)}}{40}\left(\frac{L_1}{L_3}\right)^3$

The beam characteristic coefficients in the above expressions are non-dimensional terms that are functions of the beam shape (a_0) as given below [8], along with their numerical values for $a_0 = 0.3$, a choice discussed later.

$$k_{11}^{(0)} = \frac{6}{a_0\left(3 - 6a_0 + 4a_0^2\right)} = 12.82$$

$$k_{11}^{(1)} = \frac{3\left(15 - 50a_0 + 60a_0^2 - 24a_0^3\right)}{5\left(3 - 6a_0 + 4a_0^2\right)^2} = 1.17$$

$$g_{11}^{(1)} = \frac{2a_0^3\left(105 - 630a_0 + 1440a_0^2 - 1480a_0^3 + 576a_0^4\right)}{175\left(3 - 6a_0 + 4a_0^2\right)^3} = 0.000838 \tag{4}$$

$$k_{33} = \frac{6}{a_0}\left(\frac{L_1}{T}\right)^2 = 20\left(\frac{L_1}{T}\right)^2$$

In Eq. (1), η is a dimensionless parameter that represents the effectiveness of the clamp in the C-DP-DP mechanism in overcoming the Y direction under-constraint associated with the secondary stages [10]. The condition of $\eta = 0$ corresponds to the absence of a clamp, for which the K_x expression in Eq. (1) simply reduces to that for the DP-DP mechanism. For a well-designed C-DP-DP mechanism, the value of η should be around or greater than 100.

Table 1
Physical attributes of the CDP-DP and DP-DP flexure mechanism.

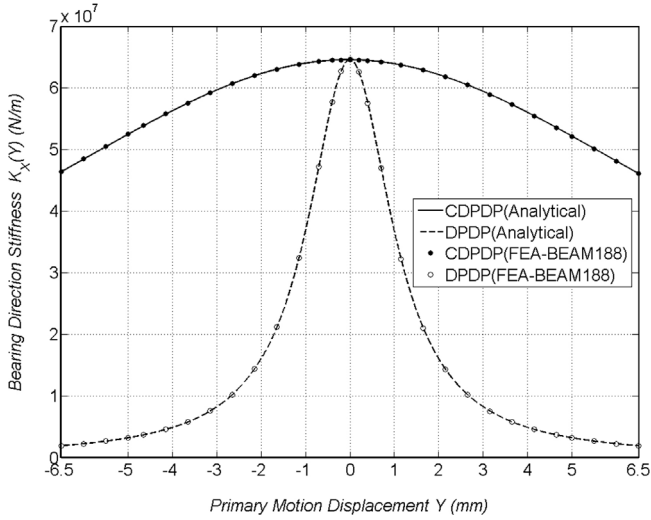| Quantity	Notation	Range/Value C-DP-DP	Range/Value DP-DP
Motion Direction Stiffness	K_y (N/m)	6982–7069	6982
Bearing Stiffness at Location 1	K_x (N/m)	4.44×10^7–6.44×10^7	0.194×10^7–6.44×10^7
Rotational Stiffness	K_θ (N.m)	6.24×10^4–7.97×10^4	6.24×10^4–7.97×10^4
Bearing Direction Displacement at Location 1	X_A (μm)	0.142–0.205	0.142–4.65
Rotational Motion	Θ (μrad)	0.415–0.672	0.295–0.793
Bearing Direction Force	F_{x1} (N)	10	10
Motion Direction Force	F_y (N)	±45.6	± 45.3
Center of Stiffness (measured to the right of location "1" in Fig. 3)	CoS (mm)	4.31 (at Y = − 6.5 mm) 3.38 (at Y = 0 mm) 2.46 (at Y = 6.5 mm)	1.60 (at Y =−6.5 mm) 3.38 (at Y = 0 mm) 5.16 (at Y = 6.5 mm)

Fig. 4. Bearing Stiffness (K_x) of the DP-DP and CDP-DP mechanisms: Closed-form vs. FEA.

Fig. 5. Center of Stiffness (CoS). Solid lines illustrate the stage after displacement due to loading.

Furthermore, setting $L_4 = 0$ in Eq. (1) reduces K_x to the previously known expressions for symmetric DP-DP and C-DP-DP mechanisms [1,8,10].

The rotational stiffness K_θ, given by Eq. (2), for the DP-DP and CDP-DP flexure mechanisms is the same and is not affected by the asymmetry (L_4). The motion direction stiffness K_y for both these flexure mechanisms is given by Eq. (3) and is also not affected by the asymmetry (L_4). In this expression, λ is a dimensionless parameter that represents the increase in K_y stiffness of the C-DP-DP mechanism with respect to the DP-DP mechanism as a result of the clamp. The condition of λ = 0 corresponds to the absence of a clamp, for which the K_y expression in Eq. (3) simply reduces to that for the DP-DP mechanism. The length L_3 of the parallelogram beams associated with the clamp can be chosen to minimize λ and therefore limit an increase in K_y stiffness.

All these closed-form relations are based on the assumption that only the flexure beams are compliant while all other stages (primary stage, secondary stages, external clamp, ground, and the middle sections of the DP flexure beams) are perfectly rigid. When the same assumptions are made in a finite elements based model (ANSYS: BEAM188 elements, NLGEOM turned on), the above closed-form results match perfectly with the finite elements analysis (FEA), as shown in Fig. 4. While these assumptions do not strictly hold in practice, which also becomes evident in the experimental work presented subsequently, the parametric nature of the closed-form relations helps select baseline dimensions without resorting to multiple iterations. A more accurate FEA (ANSYS: PLANE183 elements, NLGEOM turned on) that captures the compliance of these
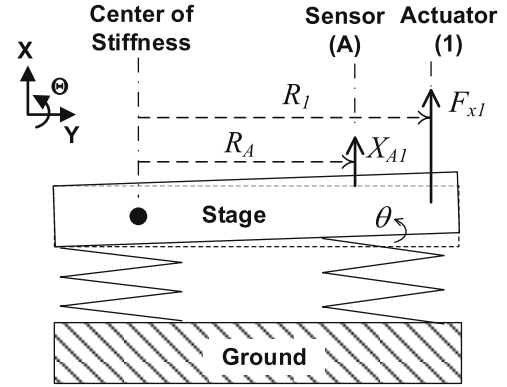
stages is used for some design decisions in Section 3, and for a direct comparison with experimental measurements in Section 5.

Referring to Fig. 3, the length $L_1 = 65$ mm and thickness $T = 0.8$ mm of the beam flexures in each DP were chosen to achieve a Y displacement range of ±6.5 mm while maintaining a safety factor of 2 against yielding. The parameter a_0 determines the degree of distributed compliance of each beam flexure and was selected to be 0.3 based on previous beam shape optimization [8,10]. The thickness of the middle sections of each beam, intended to be rigid, was chosen to be 3T to provide 27 times higher moment of area in bending compared to the flexible end-sections of the beam. The beam spacing of the inner parallelograms, $2W_1 = 49.08$ mm, is selected to reduce rotational error motions and increase rotational stiffness; beam spacing of the outer parallelograms, $2W_2 = 141.30$ mm, is selected to be greater than $2W_1$ and accommodate the external clamp. As noted earlier, the external clamp also introduces asymmetry in the design quantified by $L_4 = 34.19$ mm. The secondary stages are connected to the external clamp (length $2L_2$) via respective parallelogram flexures. Each of these parallelograms has a width $2W_3$ and the flexures in these parallelograms are of length L_3 and uniform thickness T. It should be noted that while a smaller value of L_3 is beneficial for clamp effectiveness η and K_x, this also causes an increase in λ and K_y. The dimensions associated with the clamp were chosen to be, $2L_2 = 146.9$ mm, $L_3 = 32.5$ mm, and $2W_3 = 31.7$ mm, to ensure a high enough value of η (=288) and keep the increase in K_y less than 3% from its nominal value for a Y displacement range of ± 6.5 mm.

To minimize the contribution to the X direction compliance of overall flexure mechanism from the primary stage, secondary stages, the external clamp, and the ground stages, the minimum in-plane thickness of these stages was chosen be at least 15 times larger than the thickness of the flexure beams. As a result of this choice, the initial expectation was that the X direction compliance

of the overall mechanism would be primarily dictated by the beam flexures and would not be affected by the remaining "rigid" elements of the mechanism. However, experimental measurements presented later in this paper show that despite this choice of dimensions, the compliance of some of the stages becomes relevant and cannot be ignored. This offers some new design insights and guidelines that are discussed in Section 5.

For the dimensions selected above, Table 1 provides a summary of various physical quantities (stiffness, forces, displacements, and rotations) for the CDP-DP and DP-DP flexure mechanisms based on closed-form and BEAM188 FEA predictions. These entries assume a nominal bearing direction load of 10N applied at the primary stage location "1" and for a Y displacement range of ± 6.5 mm. These quantitative estimates help in the selection of sensors and actuators.

2.2. Determination of sensing and actuation needs

Next we proceed to determine how many independent measurements are required to calculate the bearing direction stiffness (K_x) and rotational stiffness (K_θ) of the flexure mechanism at any given Y displacement position. The *Center of Stiffness* plays a very important role in this calculation [1]. For any system comprising a ground and a rigid stage interconnected by elastic elements, the *Center of Stiffness* (CoS) is that location on the rigid stage where if a force is applied, the stage only translates and does not rotate. Referring to Fig. 5, if an X direction force F_{x1} is applied at some location that is at distance R_1 from the CoS, then the X displacement at location R_A from the CoS is given by:

$$X_{A1} = X_{CoS} + R_A\theta_1 = \frac{F_{x1}}{K_x} + \frac{F_{x1}R_1R_A}{K_\theta} \tag{5}$$

Here K_x is the X direction stiffness at the CoS and K_θ is the rotational stiffness, which is independent of any reference point. Clearly, if the force is applied at the CoS (i.e. $R_1 = 0$) or the sensor is located at the CoS (i.e. $R_A = 0$) then the second term above vanishes. The above relation assumes that the ground, on which the sensor is mounted, and the stage are perfectly rigid and do not deform due to load application.

For the flexure mechanisms considered here, the location of the CoS is not known *apriori* and needs to be determined experimentally. Therefore, there are four unknowns in the above equation: K_x, K_θ, R_i, and R_A, which indicates that multiple measurements are needed.

Applying a force F_{x2} at a different location R_2 would produce the following X displacement at a different sensor location R_B:

$$X_{B2} = X_{CoS} + R_B\theta_2 = \frac{F_{x2}}{K_x} + \frac{F_{x2}R_2R_B}{K_\theta} \tag{6}$$

Displacements such as X_{A1} and X_{B2} can be measured precisely via non-contact sensors such as capacitance probes, linear encoders, or LVDTs. Note that the relative separation between the sensors and actuators, e.g. $(R_A - R_1)$, $(R_B - R_2)$, $(R_2 - R_1)$, etc., are set by the experimentalist, and are therefore known; however these locations (R_1, R_2, R_A, R_B) with respect to the CoS are unknown.

If one sets $F_{x2} = F_{x1}$ in the experiment and measures X_{A1} and X_{B2}, then subtraction of Eq. (6) from Eq. (5) yields:

$$X_{A1} - X_{B2} = \frac{F_{x1}}{K_\theta}(R_1R_A - R_2R_B) \tag{7}$$

But this does not help determine K_θ because the quantity in the parenthesis on the right hand side remains unknown even if the experiment is set up such that $R_A = R_1$ and $R_B = R_2$, or $R_A = R_B$, or $R_1 = R_2$, etc. In fact, any number of additional measurements of this kind will not help achieve the desired goal of determining K_x, K_θ and the location of CoS. One option to overcome this chal-

lenge is to apply a moment on the stage via two equal and opposite forces off-set by a known distance, resulting in a known moment, and measuring the rotation of the stage. Such an experiment would yield K_θ in a straight-forward manner, and the remaining unknowns can then be determined from measurements corresponding to Eqs. (5) and (6). However, generating a moment in this manner adds a bit more complexity in the experimental set-up.

The key observation here is that, one can first determine K_θ by measuring θ, because both these quantities are independent of point of force application and location of CoS. Experimentally, it is easy to calculate rotation from displacements at two different locations (e.g., A and B) for a given load. Also, instead of applying a pure moment, one simply needs to apply a force at two different locations (e.g., 1 and 2), one at a time, and measure the corresponding rotation for each case. Mathematically, this may be stated as:

$$\theta_1 = \frac{X_{A1} - X_{B1}}{R_A - R_B} = \frac{F_{x1}R_1}{K_\theta} \tag{8}$$

$$\theta_2 = \frac{X_{A2} - X_{B2}}{R_A - R_B} = \frac{F_{x2}R_2}{K_\theta} \tag{9}$$

Assuming that the force magnitude is kept the same for the two loading conditions in the experiments (i.e. $F_{x1} = F_{x2} = F_x$), subtracting Eq. (9) from Eq. (8) results in:

$$\frac{(X_{A1} - X_{B1}) - (X_{A2} - X_{B2})}{(R_A - R_B)} = \frac{F_x(R_1 - R_2)}{K_\theta} \tag{10}$$

Here, X_{A1}, X_{B1}, X_{A2}, and X_{B2}, are the four experimentally measured displacements; the distances $(R_1 - R_2)$ and $(R_A - R_B)$ and the force F_x are known from the experimental setup; thus, K_θ can now be determined from Eq. (10). Eqs. (8) and (9) can now be used to determine R_1 and R_2, respectively, which reveal the location of the CoS and therefore values of R_A and R_B. Next, any one of Eqs. (5) or (6) may be used to determine K_x.

Thus in summary, we conclude that to experimentally determine the K_x and K_θ stiffness:

1. The same load amount has to be applied on the primary motion stage at two distinct locations, one at a time, and for each load application, displacements have to be measured at two distinct locations on the motion stage. The sensing and loading locations need not be the same.
2. The X_{A1}, X_{B1}, X_{A2}, and X_{B2} measurements have to be repeated over the desired Y displacement range of the motion stage. It is expected that the location of the CoS, and therefore the values of locations (R_1, R_2, R_A, and R_B all vary with Y displacement. This would lead to an experimental determination of how the K_x and K_θ stiffness values vary with Y displacement. The experimental setup and procedure must ensure that the motion direction actuation does not disturb the motion stage displacement in the bearing direction.
3. Since the measured displacements are expected to be in microns, it is important that the sensing and loading (or actuation) methods in the bearing directions do not introduce any friction or backlash to the experimental setup. These sensing and actuation methods should be capable of sub-micron resolution and accuracy and should operate over a range of Y displacement of the motion stage.
4. To ensure high sensitivity in the X_{A1}, X_{B1}, X_{A2}, and X_{B2} measurements, the sensor locations A and B should be chosen as far as practically possible. This would ensure large displacements at the sensors for a given rotation, and therefore cleaner experimental data (i.e. higher signal to noise ratio). Similar, loading locations 1 and 2 should be chosen as far as practically possible to ensure a large difference between θ_1 and θ_2, which would

result in a cleaner experimental determination of K_θ from Eq. (10).

5. For the above procedure to yield accurate bearing stiffness determination, the X_{A1}, X_{B1}, X_{A2}, and X_{B2} measurements should not be affected by parasitic structural compliance of the motion stage and ground. This structural compliance cannot be completely eliminated, as noted earlier, but the experimental set-up has to be designed to minimize its influence.

These conclusions help guide the detailed design of the experimental setup in the next section. Based on the mathematical results of this section and the force-displacement data obtained from BEAM188 FEA in *Section 2.1*, the predicted CoS locations for the DP-DP and C-DP-DP flexure mechanisms are listed in Table 1. As expected, the CoS location changes with the Y displacement.

3. Detailed design of the experimental setup

The flexure mechanism, along with several assembly features and the ground frame, was designed to be monolithically fabricated on an AL6061 plate, as shown in Figs. 2 and 3, per the dimensions determined in Section 2. Wire-EDM was chosen as the fabrication method to ensure tight dimensional tolerances ($\pm 5\,\mu m$), which are critical for a reliable comparison between modeling and experimental results.

3.1. Motion direction actuation and sensing

The flexure mechanism was designed for Y displacement range of ± 6.5 mm. As per Table 1, the required motion direction actuation force is ± 45N. For this purpose, we selected a DC motor driven precision micrometer with a non-rotating tip (PhysikInstrumente DC-Mike, M-227.25). This actuator also has a built-in rotary encoder (resolution of 3.5 nm), which was used to measure the Y displacement of the primary motion stage. However, the accuracy of this measurement is limited to 2 μm by the backlash and pitch variation in the micrometer This in turn limits the point to point positioning accuracy when the actuator is operated in closed-loop using the encoder feedback. The positioning accuracy of 2 μm is acceptable, because the smallest Y displacement of interest is ± 0.5 mm.

A load cell (Model # ELFS-T3E-50L) was mounted between the actuator and the primary stage to measure the load applied by the actuator. The load cell provides a measurement range is 50 lbs which is more than adequate for the maximum predicted motion direction force; and an accuracy of ± 0.5 lb.

The ground plate was designed to include a monolithic flexure based clamp [1,16], which was used to mount the cylindrical actuator in-plane. This design provides a relatively uniform clamping force distribution, resulting in a mounting that is secure but also non-damaging to the actuator. The moving end of the actuator interfaces the primary motion stage via an actuator coupling that was designed as an extension of the primary stage. A spilt bronze sleeve between the coupling and the moving end of the actuator provides a cylindrical clamp, which is tightened via two screws. This arrangement provides a distributed clamping force without damaging the cylindrical surface of the moving end of the actuator. The thin flexure beam is included between the primary motion stage and the actuator coupling to serve as an isolator. This isolator beam transmits the Y direction force from the actuator to the primary motion stage, but at the same time absorbs any small off-axis motions between the actuator and the primary motion stage. This is important to ensure that the motion direction actuation does not apply loads on the primary stage in the X or Θ directions, thereby affecting displacements in these directions. For a thickness T value of 0.8 mm, the dimension L_5 was chosen such that the
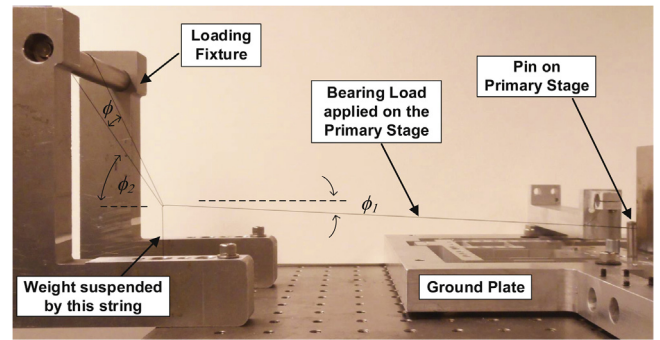

Fig. 6. Virtual Pulley Set-up.

bending stiffness of the isolator beam is several orders of magnitude less than the lowest value of the CDPDP mechanism bearing stiffness. This isolator beam, which is easily incorporated within the monolithic flexure plate design, accommodates in-plane misalignments via design, while out-of-plane misalignments are limited via tight manufacturing and assembly tolerances. A hard stop was designed into the ground plate to limit the actuator displacement to ± 6.5 mm, thereby preventing inadvertent damage to the flexure bearing.

3.2. Bearing direction actuation: Virtual Pulley

As determined in Section 2, to measure the K_x and K_θ stiffness values, X directions loads need to be applied on the primary stage at two different locations, one at a time. Furthermore, this has to be repeated over the entire range of Y displacement. Since the displacements in the X direction are very small (of the order of microns), the X direction actuation system has be free of friction and backlash, which adversely affect the accuracy and repeatability of experiment.

To accomplish this goal, one can potentially employ non-contact force actuators such as a voice coil or a moving magnetic actuator. The challenge here would be to either incorporate two actuators or use one actuator in two different locations, one at a time. An even greater challenge would be change the actuator position as with changing Y displacement of the primary stage.

Another option would be to use a high-precision displacement actuator such as a piezoelectric stack. Here the experimental design challenge would be include an isolator between the actuator and the primary stage to prevent any damage due to off-axis loads, include a load-cell to measure the force applied by the actuator, incorporate a means to independently apply forces at two locations on the primary stage, and incorporate a means to change the location of the actuator(s) with changing Y displacement of the primary stage.

While either of the above options can be implemented via appropriate hardware design, a much simpler and cost-effective alternative is to use free hanging weights. But that requires the use of a pulley to change the direction of the vertical gravitational force to a horizontal force applied on the ground plate mounted on an optics table. A traditional pulley that employs either a roller or a non-rolling pin is prone to friction and backlash, leading to measurement hysteresis, and is therefore inadequate for this testing.

To overcome this challenge, we propose the novel concept of a virtual pulley: a geometric arrangement of strings that provides the functionality of a pulley (i.e. changes the direction of a tension bearing string) without actually using a physical pulley. This idea, illustrated in Fig. 6, has been suggested in the past [1], but the current work is its first reported practical implementation.

One of the strings is attached to a loading fixture that overhangs the edge of the optics table. This string is looped around a steel rod on the fixture as shown in Fig. 6. A second string is tied to the loading point on the primary stage, then threaded through the loop of the first string, and subsequently attached to a hanging weight. In our experiment, each of these strings is a 302 stainless steel braided cable with 1×7 strand construction, 0.012 in diameter, 25 lb breaking strength. The system achieves an equilibrium state under the gravitational force and the spring force of the flexure bearing. Using basic trigonometric relations and measurements of the string angles, one can determine the X direction force F_x in terms of the known weight W.

$$F_x = \frac{W}{\frac{\sin\phi_2 + e^{\mu\theta}\sin(\phi+\phi_2)}{\cos\phi_2 + e^{\mu\theta}\cos(\phi+\phi_2)} - \tan\phi_1} \qquad (11)$$

A fixed weight $W = 1.5$ kg was used for all the experiments. Angles ($\phi = 8.5°$, $\phi_1 = 4°$, $\phi_2 = 54°$) were measured from distortion-free side view images of the set-up (similar to Fig. 6). The term $e^{\mu\theta}$ accounts for the difference in the tension due friction one two sides of the string wrapped around the cylindrical steel rod in the loading fixture. The angle of wrap (θ) of the first string around the steel rod was measured from a side view image to be 190°. The coefficient of friction (μ) between the string and the rod was experimentally determined to be 0.15 ± 0.005. The interfaces between the two strings and between the first string and the steel rod are non-sliding interfaces, held in place by static friction. Therefore, there is no hysteresis in the resulting measurements. However, relying on static friction to hold an interface introduces a small error in the X direction force F_x for a given weight W, as indicated by Eq. (11) and captured later in Section 5.3. Alternatively, these interfaces could have been locked using glue or knots, which not only eliminate hysteresis but also reduce measurement error.

Furthermore, per the conclusions of Section 2.2, these two locations were chosen to be as far away from each other as possible and yet kept close to bases of the inner parallelogram flexure beams (marked by * in Fig. 3) to minimize any deformation of the primary stage. The primary stage had two pressed dowel pins corresponding to the two points of load application (1 and 2). To change the set-up between the two load applications, the first string was simply switched from one pin to the other while the looped second string was slid along the length of the steel rod on the loading fixture, such that both strings were in a single plane normal the Y motion axis of the flexure bearing.

The use of the virtual pulley concept reduced the cost and complexity of the experimental set-up while providing high precision measurements. In general, this kind of arrangement is suitable when displacements are small. While the above-described method is one way of setting up the virtual pulley, one can envision various alternate ways to accomplish a similar geometric arrangement.

3.3. Bearing direction sensing

As determined in Section 2.2, the X displacement of the primary stage has to be measured at two locations. Non-contact sensors are ideal for this purpose because they do not contribute any friction or backlash. Furthermore, to avoid re-mounting the X displacement sensors for each Y displacement of the primary stage, the sensors should be insensitive to the latter. Capacitance probes meet all these criteria and were therefore selected. Furthermore, to maximize the sensitivity of measurement, the two capacitance probes were spaced (locations A and B) as far apart as possible. To achieve this, the primary stage was designed with an extended arm. Since this arm does not lie in the load path, it does not get deformed during the loading experiments.

The two capacitance probes mounted at locations A and B were from Lion Precision (Model C-1A, Full Scale Range: $500\mu m$, RMS Resolution: 8.6 nm, Accuracy: 19 nm based on uncertainty of calibration, Sensitivity 0.04 V/μm). The sensor system consists of three components: capacitance sensor, capacitance signal amplifier and a sensing surface. The capacitance sensors were mounted on respective fixtures attached to the ground frame and the sensing surfaces were precision ground gage blocks that were attached to the primary stage.

The probe mounting fixtures were attached to the ground frame at locations that were determined to have minimal deformation under loading. Even though the ground plate is designed to be stiff, certain segments are more compliant than others because of their geometry. This parasitic compliance can lead to several microns of displacement, thereby corrupting the X displacement measurement. As discussed in the next sub-section, FEA was used to predict the deflection of the ground frame under bearing direction load for the entire range of Y displacement of the primary stage. The deflection results from the simulation were used to choose a set of points (G2) on the ground frame (see Fig. 2) that had deflections that were at least two orders of magnitude less than the bearing direction deflections of the CDPDP flexure mechanism.

3.4. Ground mounting

The choice of screw locations to mount and secure the ground plate to the optics table is a crucial decision in the experimental set-up design because this determines the extent to which ground compliance plays a role. Two choices were considered — three G1 holes or four G2 as shown in Fig. 3 — and compared with a perfectly ideal ground via FEA. To capture the compliance of the ground plate and various stages in the flexure mechanism, the planar geometry of shown in Fig. 3 was meshed using PLANE 183 elements in ANSYS. The PLANE183 element (8 nodes and 16° of freedom) accurately captures large deflections and associated non-linearities when the NLGEOM option is enabled. For planar geometries like those being considered here, PLANE183 provides greater computational efficiency compared to 3D solid elements.

To serve as a baseline, "ideal ground" was modeled by setting zero displacement boundary conditions at the locations where the four beams associated with the two outer parallelograms in both the DP-DP and C-DP-DP flexures interface with the ground plate (marked by the signs Δ in Fig. 3). This eliminates the effects of any compliance associated with the ground plate, which is also equivalent to assuming a perfectly rigid ground plate. For the G1 and G2 mounting locations, the actual geometry of the ground plate was modeled with displacements at the screw hole locations set to zero. In each case, a 10N force in the X direction was applied at loading location 1. Fig. 7a and b show the FEA generated deformation maps of the C-DP-DP ground plate for screw locations G1 and G2, respectively.

Furthermore, Fig. 8 shows the FEA predicted X_{A1} deflection of the primary stage with varying Y displacement, under an X direction load of 10N at location 1, for the various ground options. From Fig. 7, it is clear the G1 screw location results in significant ground plate distortion, which moves the probe mounting fixture location. This adversely affects the X direction displacement measurement of the primary stage with respect to the ground plate, as seen in Fig. 8. The ground plate distortion and the resulting corruption of the capacitance probe displacement measurements render the assumptions and conclusions of Section 2.2 invalid. Moving the screw location from G1 to G2 substantially mitigates these effects but does not completely eliminate them. The G2screws are located on the ground plate as close as practically possible to the base of the outer parallelogram flexure beams (marked by the signs Δ in Fig. 2); nevertheless, the small segment of ground plate in-
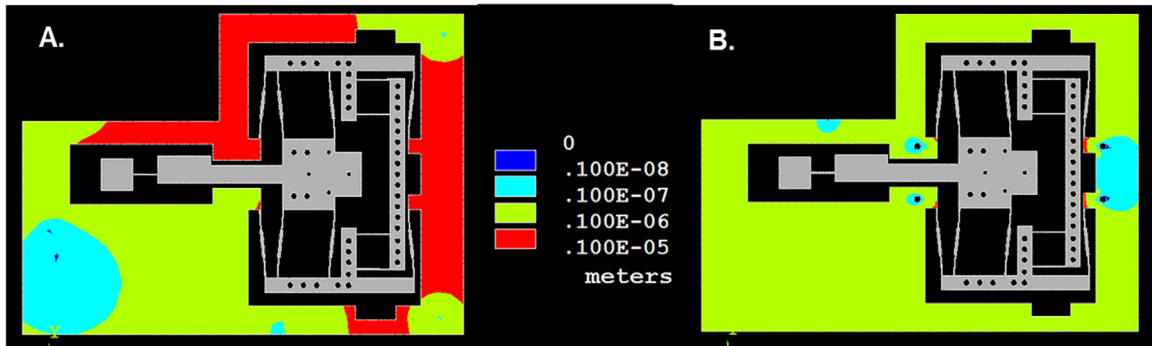
Fig. 7. C-DP-DP Ground Plate Deformation Map (a) Screw Location G1 (b) Screw Location G2.
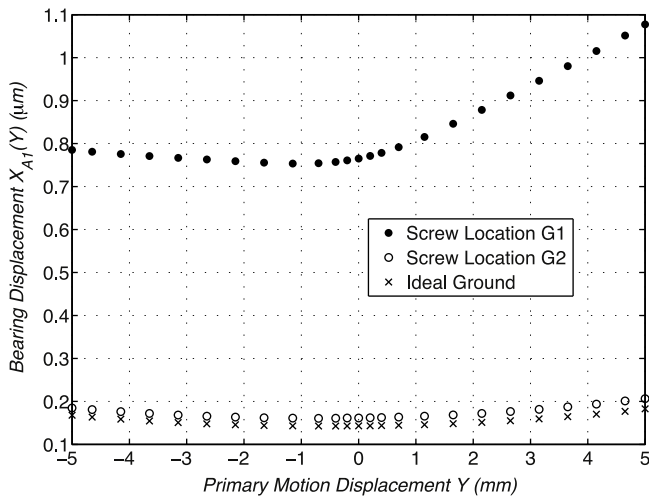

Fig. 8. Bearing Direction Displacement $X_{A1}(Y)$: FEA predictions for various ground options.

between contributes a finite ground compliance resulting in the small discrepancy seen in Fig. 8. It is clear that ground mounting plays a key role in the overall system compliance: the G1 option results in almost an order of magnitude greater bearing direction displacements at the primary stage compared to the G2 option. We concluded that despite the small discrepancy compared to ideal ground, G2 represents the best ground mounting option that separates the actuation load loop and metrology loop and can be practically implemented in the experimental set-up. Accordingly, ground plate was mounted on a Newport RS1000 optics table using ¼-20 screws at the G2 location. Four Mitutoyo gage blocks (0.15 inch thickness) with through holes for the mounting screws provided consistent spacing between the ground plate and the table top. A separate FEA showed an insignificant impact of the Y actuation force on the plate distortion.

3.5. Data acquisition and control system

A real-time control prototyping system DS1103 from dSPACE was used to command and control the Y direction actuator and to acquire and store data from all sensors in the system.

4. Experimental procedure and data

Even though the flexure mechanism was designed for ±6.5 mm motion range, the experimental data was collected over a range of ±5 mm, which is adequate for the current investigation. We conducted an initial round of experimental measurements using a two-step procedure. In the first step, the primary stage was moved

from Y = −5 mm to +5 mm in 0.25 mm steps without any bearing direction load, and the bearing direction displacement at locations A and B was captured at each Y displacement position. In the second step, the same process was repeated, but with the bearing direction load applied at location 1 and 2 (one at a time). The difference between the displacements with and without the bearing load was used to calculate X_{A1}, X_{B1}, X_{A2}, and X_{B2}. However, drift in the capacitance probe measurements posed a serious limitation to using this two-step procedure, resulting in inconclusive data. To characterize this drift, the output of the capacitance probes was recorded over 30 min, with the experimental set-up left in steady state. Over multiple such 30 min durations at different times in the day and over several days as well as for various loaded and unloaded conditions, the capacitance probe drift ranged from 1 nm to 180 nm. This level of drift and associated uncertainty is unacceptable, given that some of the expected displacement levels are in the same range (Table 1). To overcome the effects of drift without resorting to stringent environmental control, we developed an alternate experimental procedure, which is outlined below.

As earlier, the primary stage was moved from Y = −5 mm to +5 mm in 0.25 mm steps. For each Y position, a bearing direction load F_{x1} was applied at location 1 by adding W = 1.5 kg weight to the loading string of the virtual pulley. The weight was left hanging for 30 s to allow any transients to die out. Next, the string was unloaded by simply lifting the weight manually and kept that way for another 30 s to let the new transients to die out. The loading and unloading, each with a 30 s hold, was repeated five times. The output measurements from both probes, A and B, were recorded for this entire duration. Then, the primary stage was moved to the next Y position and the above loading/unloading steps and associated measurements were repeated. Fig. 9 shows a representative position output from capacitance probe A at Y = −1.75 mm and Y = −1..5 mm. The output was filtered using a moving average over 50 samples to reduce measurement noise. From this data, we were able to measure the delta in primary stage position with and without bearing load (i.e. X_{A1} and X_{B1}). Since this delta happens over a very small period of time, there is practically no effect of drift. Also, any bearing direction error motion that exists independent of the loading also gets eliminated from the measurement. Furthermore, repeating the loading/unloading five times allows an average of the measurement, reducing random errors.

The same procedure was repeated for the bearing load position 2, resulting in measurements of X_{A2} and X_{B2} as a function of Y displacement. Although the loading and unloading was done manually by hanging and lifting the weights, this process can also be automated if needed.

Fig. 10 shows the primary stage bearing displacement measurement, X_{A1}, at probe A for the C-DP-DP flexure mechanism in response to the bearing load F_{x1} = 8.46N (W = 1.5 kg), for one complete experimental run of Y = −5 mm to +5 mm. Also shown for

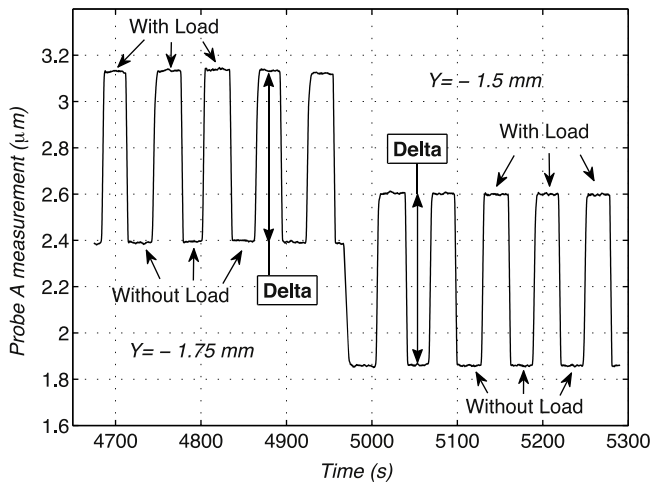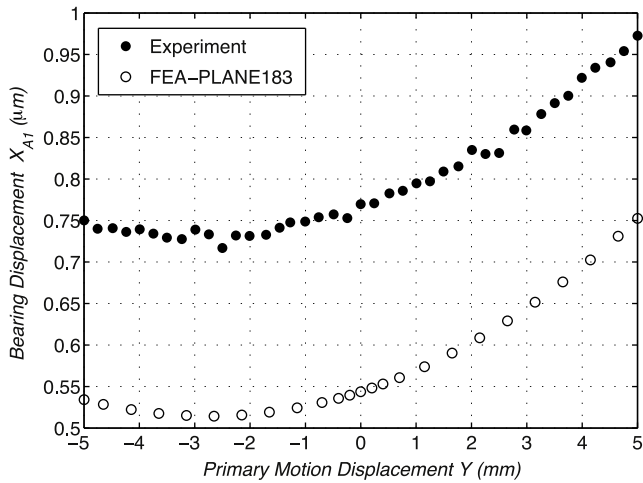**Fig. 9.** Probe A Measurement for Y = −1.75 mm and −1.5 mm.

Fig. 10. Bearing Direction Displacement $X_{A1}(Y)$: Experiment versus FEA.
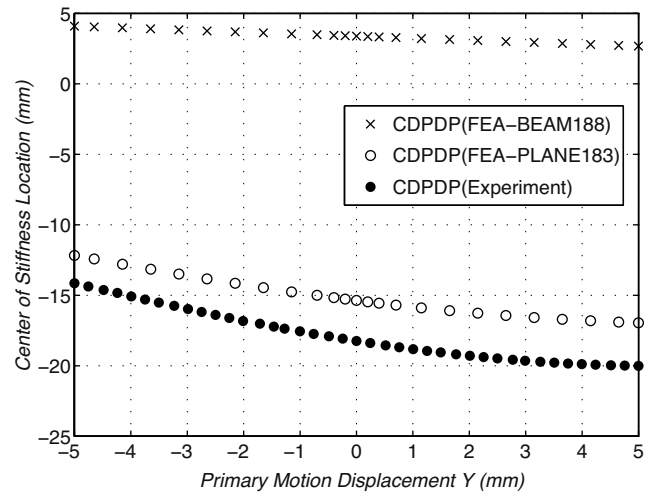

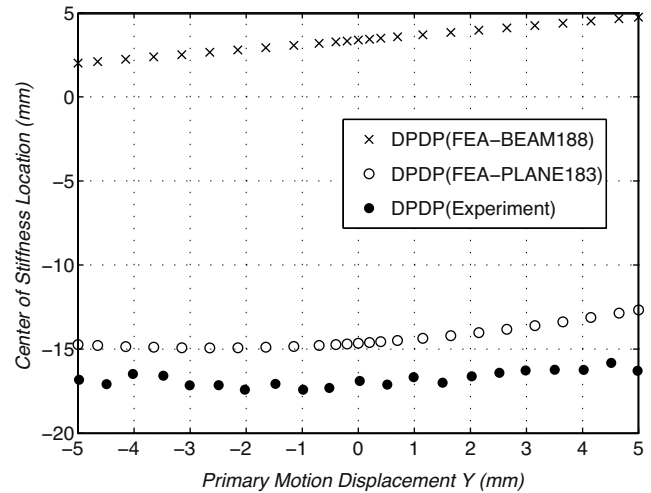**Fig. 11.** Center of Stiffness Location for the C-DP-DP mechanism.

Fig. 12. Center of Stiffness Location for the DP-DP mechanism.

comparison is an FEA (PLANE183) prediction for the same ground option (G2), loading condition, and sensor location. The discrepancy seen here will be discussed in the next section. Similar data was compiled for X_{B1}, X_{A2}, and X_{B2} as well. Additionally, force F_y was measured via the load cell and associated displacement Y were measured using the optical encoder embedded with the Y actuator.

5. Results and discussion

5.1. Bearing and rotational direction stiffness

Once the displacements X_{A1}, X_{B1}, X_{A2}, and X_{B2} were experimentally measured, the expressions from Section 2.2 were used to determine the Center of Stiffness (CoS) and stiffness values K_x and K_θ for each flexure mechanism. In this section, these experimental results are compared with BEAM188 based FEA (described in Section 2.1) and PLANE183 based FEA (described in Section 3.4). BEAM188 based FEA model assumes the various stages in the mechanisms (primary stage, secondary stages, external clamp, ground, and the middle sections of the DP flexure beams) to be perfectly rigid. These simplifying assumptions are removed in the PLANE183 based FEA, which represents the most accurate model of the actual physical system and is therefore best-suited for comparison with the experimental results.

Figs. 11 and 12 plot the variation of the CoS location with Y displacement for the C-DP-DP and DP-DP mechanisms, respectively. The CoS location, measured to the right with respect to point "1" in Fig. 3, was calculated using data obtained from BEAM188 based FEA, PLANE183 based FEA, and experiments.

As expected, while the BEAM188 based FEA prediction does not match very well with the experimental measurement, the PLANE183 based FEA offers a better match for each mechanism. Although there remains a finite discrepancy between PLANE183 and experiment, which is discussed later, the trends and orders of magnitude clearly match.

Next, the bearing direction stiffness (K_x) determined from PLANE183 FEA and experiments are plotted against the motion direction displacement Y for the C-DP-DP and DP-DP mechanisms in Fig. 13. Note that for each value of Y, stiffness K_x is reported at the Center of Stiffness, which itself varies with Y as seen above. There are several key observations here. For each mechanism, a comparison between PLANE183 FEA and experiment shows that the K_x order of magnitude and trend match well. As discussed later, the finite discrepancy arise largely from a single factor, a mismatch in the bearing direction compliance at Y = 0. Fig. 13 also provides a clear experimental validation that while the K_x bearing stiffness value at Y = 0 is the same for both mechanisms, its drop with increasing Y displacement is significantly less in the C-DP-DP
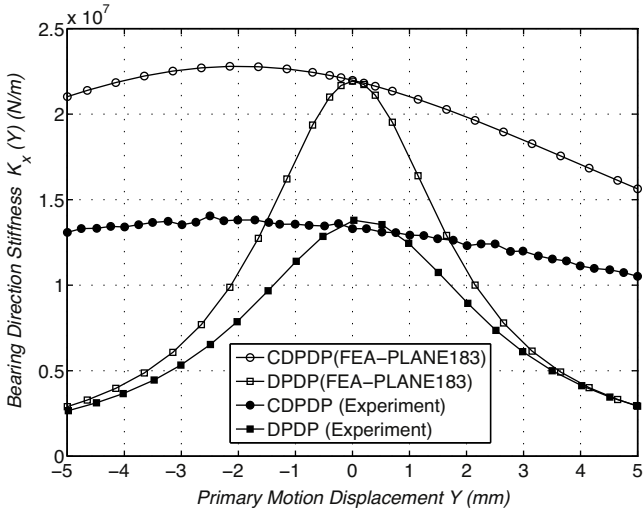
Fig. 13. Bearing Stiffness (K_x) of the CDP-DP and DP-DP mechanisms: FEA vs. Experiment.
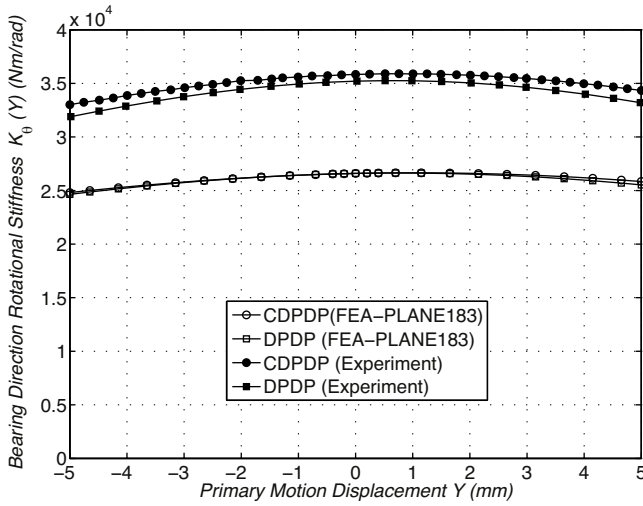

Fig. 14. Rotational Stiffness (K_θ) of the CDP-DP and DP-DP mechanisms: FEA vs. Experiment.

mechanism compared to the DP-DP mechanism. This corroborates previous qualitative and quantitative predictions.

Next, the rotational stiffness (K_θ) is plotted as a function of motion direction displacement Y for the C-DP-DP and DP-DP mechanisms in Fig. 14. Comparison between PLANE183 FEA prediction and the experimental measurement shows a good match in the order of magnitude as well as trend. The finite discrepancy between the prediction and measurement, as discussed later, is primarily due to a mismatch in the rotational compliance at $Y=0$. Also, these measurements confirm that the external clamp in the C-DP-DP mechanism does not affect the rotational stiffness and its variation, which remain the same as that for the DP-DP mechanism. Both PLANE183 FEA prediction and experimental measurement of the stiffness is less than that predicted by closed form analysis (Eq. (2)) and BEAM188 FEA, because of the idealized assumptions made in the latter models.

It was shown in Section 2.1, as well as in prior publications [8,10], that the K_x and K_θ stiffness values calculated analytically, given by Eqs. (1) and (2), exactly match those determined using BEAM188 FEA models for the C-DP-DP and DP-DP flexure mechanisms. However, both PLANE183 FEA prediction and experimental measurement of these stiffness are less than that predicted by

closed form analysis (Eq. (1) and (2)) and BEAM188 FEA, because of the idealized assumptions made in the latter models. Thus, while these models are appropriate for basic estimation and conceptual design work, one needs to take into account the finite compliance of the ground plate, the primary and secondary motion stages, the external clamp (in case of C-DP-DP), and the middle section of beam flexures for a more accurate prediction. When this is done via the PLANE183 FEA, we see a reasonably good agreement with the experimental measurements. While running the PLANE183 FEA, we selectively turned on the finite stiffness of the various stages in all possible combinations and determined that, for the flexure geometry at hand, the biggest source of stiffness discrepancy between the closed-form/BEAM188 FEA and the PLANE183 FEA comes from the bending compliance of the ground plate and the secondary stages. The effect of the former was mitigated by moving the ground mounting from G1 location to G2 location, as discussed in Section 3.4. This reinforces the design guideline that ground anchor points should be made as close as practically possible to the base of the flexure beams. The latter issue pertaining to the secondary stages was addressed in Section 2.1, where the in-plane thickness of these stages was chosen to be 15 times that of the beam flexures to mitigate their compliance. But a comparison between the BEAM188 FEA, PLANE183 FEA, and experiment (Figs. 11 and 12), shows that this dimensional choice is still inadequate. Therefore, greater thickness should be chosen (along with appropriate trussing to manage weight) such that bearing direction compliance contribution from the secondary stages is an order of magnitude smaller than that from the beam flexures. However, if these steps pertaining to the ground mounting and secondary stage dimensions are not practically feasible, then the compliance of the ground plate and secondary stages should be taken into consideration in the modeling and design of the flexure mechanism.

Next, we proceed to systematically quantify the discrepancy seen between the PLANE183 FEA prediction and the experimental measurement. It is evident from the expressions of Eqs. (1) and (2) that the analytically derived compliance in the X and Θ directions can be expressed as quadratic functions of displacement Y. This implies that the corresponding stiffness values may be generically stated as follows:

$$K_x(Y) = \frac{1}{C_2(Y - C_1)^2 + C_0} \tag{12}$$

$$K_\theta(Y) = \frac{1}{D_2(Y - D_1)^2 + D_0} \tag{13}$$

Rather than compare the absolute values of the stiffness obtained from PLANE183 FEA and experiments, we compare the individual coefficient (C_0, C_1, C_2) and (D_0, D_1, D_2), which capture specific physical significance. Using the example of K_x: C_0 captures the purely elastic compliance at $Y=0$; C_1 contributes a linear component in Y and represents any offset in the Y reference position; and, C_2 captures the elastokinematic compliance which is quadratic in Y. The stiffness data obtained from PLANE183 FEA and the experiments are fitted with the functions given by Eqs. (12) and (13). The PLANE183 FEA data fits perfectly with this analytic function, while for the experimental data we employ a least squares fit. The resulting coefficients are summarized in Tables 2 and 3 for the C-DP-DP and DP-DP flexures, respectively, along with differences between PLANE183 FEA and experiment expressed in absolute or percentage.

The quadratic terms C_2 and D_2 in the stiffness expressions K_x and K_θ for both mechanisms predicted by PLANE183 FEA and obtained from the experimental data agree within 5%. This is within the range of experimental error as discussed later in Section 5.3. This agreement presents a strong experimental validation of the quadratic non-linearity that leads to the drop in the bearing stiffness (K_x

Table 2
C-DP-DP Compliance Coefficients: Experiment vs. FEA.

	$C_2(m/N.\mu m^2)$	$C_1(\mu m)$	$C_0(m/N)$	$D_2(rad/Nm.\mu m^2)$	$D_1(\mu m)$	$D_0(rad/Nm)$
Experiment	4.29×10^{-16}	-2214.45	7.25×10^{-8}	7.24×10^{-14}	808.01	2.77×10^{-5}
PLANE183 FEA	4.11×10^{-16}	-1995.13	4.39×10^{-8}	7.60×10^{-14}	1052.63	3.75×10^{-5}
Difference	4.38%	-219.32	65.28%	-4.74%	-244.62	-26.29%

Table 3
DP-DP Compliance Coefficients: Experiment vs. FEA.

	$C_2(m/N.\mu m^2)$	$C_1(\mu m)$	$C_0(m/N)$	$D_2(rad/Nm.\mu m^2)$	$D_1(\mu m)$	$D_0(rad/Nm)$
Experiment	1.14×10^{-14}	158.33	7.23×10^{-8}	9.40×10^{-14}	659.57	2.84×10^{-5}
PLANE183 FEA	1.19×10^{-14}	12.98	4.56×10^{-8}	9.1×10^{-14}	769.23	3.75×10^{-5}
Difference	-4.20%	145.35	58.59%	3.3%	-109.66	-24.27%

and K_θ) with increasing Y displacement, which is the primary phenomenon of interest in this investigation. These quadratic terms represent a geometric non-linearity that arises from finite displacements, as distinct from infinitesimal displacement analysis. These results also provide a direct experimental validation of the FEA and closed-form analytical predictions that the drop in K_x bearing direction is significantly less for CDP-DP mechanism as compared to the DP-DP mechanism.

The discrepancy between PLANE183 FEA and experiment in the linear terms C_1 and D_1 for both mechanisms is presented in Tables 2 and 3 as an absolute difference instead of percentage. For a flexure mechanism geometry that is perfectly symmetric about the $Y = 0$ point and an experimental set-up that precisely captures this reference point, both the linear term coefficients C_1 and D_1 would be zero. However, as described in Section 2.1, there is an asymmetry in the geometry of both mechanisms along the Y axis, captured by the finite L_4 dimension, due to the presence of the external clamp. This asymmetry is further compounded when the compliance of the various stages is taken into consideration as in case of the PLANE183 FEA. All these factors result in non-zero predicted value of C_1 and D_1 for both mechanisms, as listed in Tables 2 and 3. However, the experimentally determined values of these coefficients are slightly different. These differences are readily attributable to the error in setting the $Y = 0$ reference in the experiments. The initial position of the stage was set manually and therefore has a potential for error in the range of $\pm 500 \mu m$. The differences in C_1 and D_1 coefficients between FEA prediction and experiments are well within this range. One way of eliminating this error in the future would be to use a highly accurate pre-calibrated load cell in the Y direction to determine the true $Y = 0$ position of the flexure mechanisms.

Next, we consider the C_0 and D_0 terms, which represent the biggest discrepancy between the PLANE183 FEA predication and experimental measurements for both mechanisms. Discrepancy in these terms represents a constant offset, independent of Y, in the corresponding compliance, which is equivalent to a discrepancy in the nominal linear elastic stiffness at $Y = 0$ predicted by the infinitesimal displacement analysis. The constant offset in compliance is a direct consequence of the constant offset of approximately $0.2 \mu m$ in bearing direction displacement seen in Fig. 10. In the experimental measurement of bearing direction displacement, there is an additional component of displacement, proportional to the bearing direction force, but independent of Y position. This implies that the experiments consistently show higher compliance (constant offset independent of Y) and lower stiffness (at $Y = 0$), compared to FEA predictions for all the cases listed in Tables 2 and 3. While these discrepancies are substantial, they are to be expected because the actual manufactured geometry of the flexure mechanism always has some deviations from the ideal geometry as modeled in CAD and FEA. The ideal geometry assumes perfectly uniform thickness of all flexure beams, perfect straightness of each beam, and perfect parallelism/orthogonality between various beams and other geo-
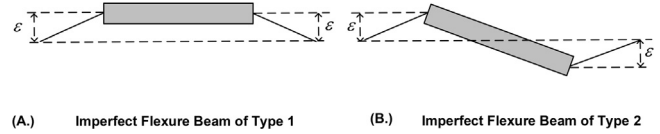

Fig. 15. Possible fabrication imperfections in beam flexure geometry.

metric features in the mechanism. Towards this end, wire-EDM was employed as the method of fabrication, which offers very tight tolerances (typically $\pm 5 \mu m$) and therefore some predictability in the manufactured mechanism's geometry. But another factor that plays a key role in determining the flexure mechanism's manufactured geometry is material stresses. When a flexure mechanism is cut out of plate stock, there is the possibility of material stresses getting relieved, which results in unpredictable deformations of the thin flexure beams. To minimize this phenomenon, a specific temper of Aluminum, AL6061-T651, was selected, where the (-51) extension signifies that the plate stock is stress-relieved but this does not always eliminate all material stresses. Therefore, it is highly probable that the resulting flexure beams post wire-EDM were not perfectly straight. In the absence of a direct characterization of the beam geometry using a coordinate measuring machine (CMM) or visual inspection via an optical comparator, we tested the hypothesis of non-straight beams via FEA modeling. We assumed two representative non-ideal geometries (Fig. 15), where the parameter ε captures the extent of geometric imperfection. Both the DP-DP and C-DP-DP mechanisms were modeled via PLANE183 FEA, while assuming the Type 1 and Type 2 imperfection, one at a time, in each flexure beam. The results showed that for a ε value of $0.5T$ in the C-DP-DP flexure mechanism, there is an additional constant X_{A1} displacement of 194 nm for Type 1 imperfection and 302 nm for Type 2 imperfection, compared to the perfect geometry. A geometric imperfection of $\varepsilon = 0.5T$ is quite possible with the current choice of material and fabrication method, and the predicted displacement discrepancy is comparable to that seen in Fig. 10. Thus, while the Type 1 and Type 2 geometries are merely representative, they help support the hypothesis that the discrepancy seen in the C_0 and D_0 coefficients may be explained by typical fabrication imperfection in the flexure beams.

5.2. Bearing direction stiffness measurement error and sensitivity analysis

To estimate the error in the experimental measurement of K_x and K_θ, we conducted a sensitivity analysis based on the propagation of errors. A partial derivative of Eq. (11) helps express fractional error in bearing force measurement, $(d F_x)/F_x$, in terms of the fractional error in the direct measurement of string angles, coefficient of friction, and weight. Similarly, a partial derivative of Eq. (10) provides the fractional error in rotational stiffness, $(d K_\theta)/K_\theta$, in

Table 4
Fractional Errors in Direct and Derived Measurements.

Quantity	Error [Units]	Source	Fractional Error [%]
Weight: W	0.001 [kg]	Accuracy per calibration record	
String Angles: ϕ, ϕ_1, ϕ_2	0.2 [deg]	Accuracy of image processing	
Distances: $(R_1-R_2), (R_A-R_B)$	0.02 [mm]	Accuracy of calipers	
Displacements: $X_{A1}, X_{B1}, X_{A2}, X_{B2}$	19.2 [nm]	Combined uncertainty per calibration record	
Bearing Force: F_x	0.36 [N]	Derived	1.6%
C-DP-DP Cos Location: R_1, R_2, R_A, R_B	1 [mm]	Derived	6.2%
DP-DP CoS Location: R_1, R_2, R_A, R_B	1 [mm]	Derived	6.3%
C-DP-DP Rotational Stiffness: K_θ		Derived	7.7%
DP-DP Rotational Stiffness: K_θ		Derived	7.6%
C-DP-DP Bearing Stiffness: K_x		Derived	6.8%
DP-DP Bearing Stiffness: K_x		Derived	4.5%

terms of fractional errors in the direct measurement of capacitance probe displacements and sensing and actuation location separation distances, as well as derived measurement of the bearing force. A partial derivative of Eq. (8) provides the fractional error in the location of CoS captured via $d(R_1)/R_1$ in terms of the fractional errors in the direct measurement of capacitance probe displacements and sensing location separation distance, as well as derived measurement of the bearing force and rotational stiffness. Finally, a partial derivative of Eq. (5) provides the fractional error in the bearing stiffness measurement, $(d K_x)/K_x$, in terms of the fractional errors in the derived measurement of CoS location, bearing force, and rotational stiffness. A summary of absolute and fractional errors in various direct and derived measurements are compiled in Table 4. Since various measurements vary with the Y displacement, average values are provided where relevant.

5.3. Bearing direction error motions

The sensor measurements at locations A and B in the absence of any bearing direction load F_x also reveal the X direction error motion (E_x expressed at the CoS) and the rotational error motion (E_θ expressed CCW positive) as a function of Y displacement. Although both the CDP-DP and DP-DP mechanisms are symmetric about the Y axis by design and therefore theoretical values of E_x and E_θ should be zero, in practice many factors contribute to non-zero values of these error motions. These factors include imperfection in the fabricated flexure mechanism geometry, imperfect application of the motion direction force F_y, angular misalignment of the capacitance probe axis with respect to the Y axis of the mechanism, and angular misalignment of the target blocks with respect to the Y axis of the mechanism. Of these, the former two are imperfections inherent to the mechanism and actuation that we seek to measure. As shown in previous work [17], misalignment of the probe axis results in a cosine error that is negligible for angles in the range of a few degrees, while similar misalignment of the target block leads to a sine error that can be significant. Straightness or flatness of the target block, which is in the range of a fraction of a micron, is ignored in this analysis since the measured errors are in tens of microns. In the context of Fig. 5, assuming a target block misalignment of β_A (measured CCW positive; not shown in Fig. 5) at sensor A, as the motion stage moves along the Y axis, the displacement measured by this sensor can be expressed as:

$$X_A = E_x + R_A E_\theta - Y\beta_A \qquad (14)$$

Assuming an analogous X direction displacement expression for sensor B, one can readily derive:

$$E_x - \frac{Y(R_A\beta_B - R_B\beta_A)}{R_A - R_B} = \frac{R_A X_B - R_B X_A}{R_A - R_B} \qquad (15)$$

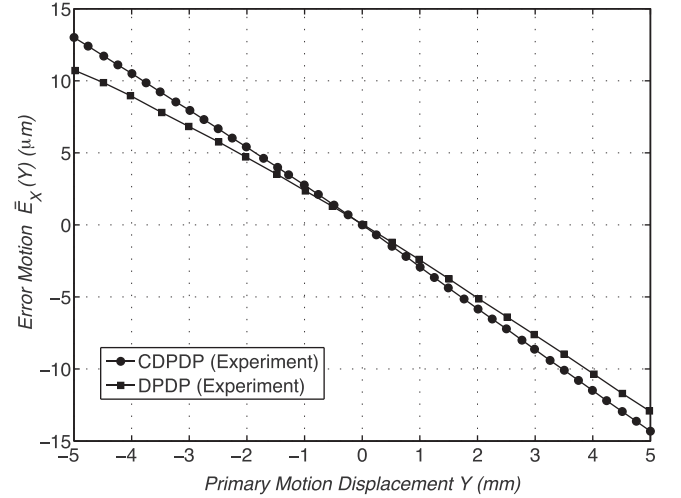$$E_\theta - \frac{Y(\beta_A - \beta_B)}{R_A - R_B} = \frac{X_A - X_B}{R_A - R_B} \qquad (16)$$

Fig. 16. Modified X Error Motion ($\bar{E}_x$) at CoS for the CDP-DP and DP-DP mechanisms.

In Eq. (15), the left hand side (LHS) is a combination of the error motion term that we seek to measure (E_x) and a term arising from the target block misalignment (β_A and β_B). As shown previously [17], these two terms cannot be distinguished in a measurement unless one measures the target block misalignment explicitly, for example with a coordinate measurement machine. Since such measurement was not available at the time of this experiment, we report the overall LHS as a modified error $\bar{E}_x$ determined by the measured quantities on the right hand side (RHS) of this equation. Thus, $\bar{E}_x$, which is plotted with respect to Y displacement in Fig. 16 for both mechanisms, represents error in the mechanism, actuation, as well as sensor target misalignment (i.e. errors associated with the experimental hardware). Analogously, a modified error $\bar{E}_\theta$, defined by the LHS of Eq. (16), is plotted with respect to Y displacement in Fig. 17 for both mechanisms. These error measurements are within the range of expected manufacturing and assembly imperfections and target block misalignment. The fact that both measured errors are almost identical for the CDP-DP and DP-DP mechanisms corroborates that the source of these errors is in the experimental hardware and setup, which is common for the two mechanisms. The fractional errors in the estimates of E_x and E_θ are computed via propagation of errors (similar to Section 5.3), and are 1.8% and 0.2% respectively.

5.4. Motion direction stiffness

The motion direction stiffness K_y for both the flexure mechanisms was experimentally determined from the F_y force and Y displacement measurements, and compared to the value predicted by Eq. (3). A comparison between the analytical predication and experimental measurement for the C-DP-DP mechanism in Fig. 18
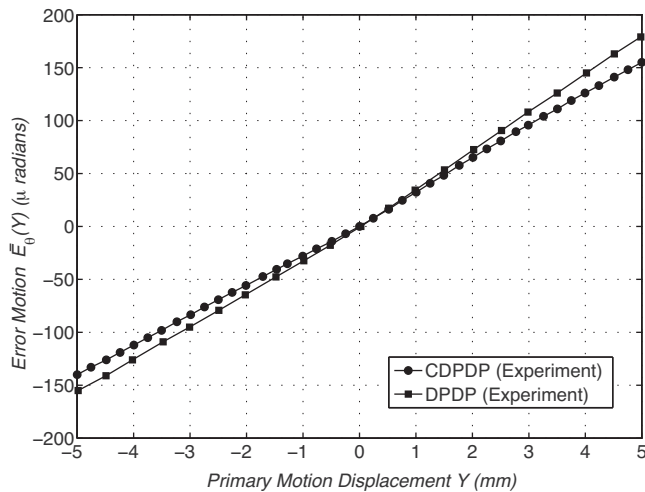
Fig. 17. Modified Rotational Error Motion ($\bar{E}_\theta$) at CoS for the CDP-DP and DP-DP mechanisms.
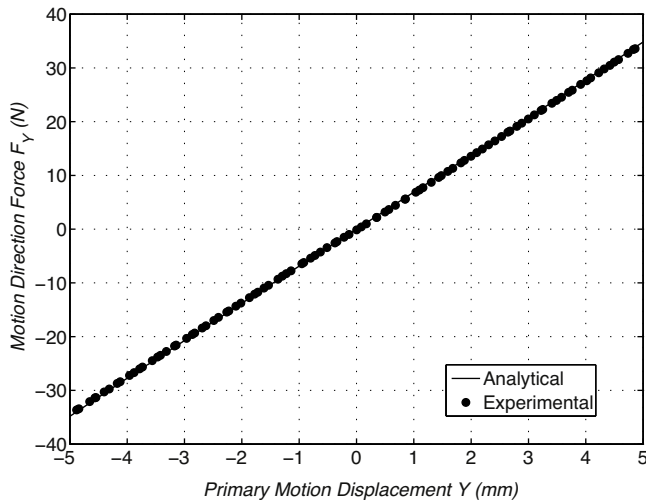

Fig. 18. Motion Stiffness (K_y) of the C-DP-DP mechanism: Analytical vs. Experimental.

shows an agreement within 1.5%. This confirms the accuracy of the analytical prediction, and shows that the external clamp in the C-DP-DP flexure, when designed appropriately with a low value of λ in Eq. (3), does not adversely impact the motion direction stiffness. For the analytical prediction, the flexure dimensions are as listed in Section 2.1 and Young's modulus of AL-6061 was assumed to be 68.9 GPa.

6. Conclusion

The original contributions of this paper are summarized at the end of Section 1. The main conclusions that we draw from this experimental work are:

1. The C-DP-DP geometry indeed overcomes the under-constraint of the secondary stages in the DP-DP flexure, resulting in significant improvement in the bearing direction stiffness without impacting motion direction stiffness. However, the experimentally measured bearing direction stiffness for both the DP-DP and CDP-DP flexure mechanisms is lower than their respec-

tive theoretical values predicted by closed-form analysis or BEAM188 FEA. This is because these idealized models do not take into account the parasitic compliance of supposedly "rigid" stages and ground mounting. Once these factors are taken into consideration via a more representative PLANE183 FEA, the experimental measurements agree well with the predictions. Any remaining discrepancy can be attributed to manufacturing tolerances and imperfections.

2. The choice of ground mounting locations is critical to minimize the impact of the ground plate compliance on the measured bearing direction deflections and therefore stiffness. Furthermore, since the ground plate also provides mounting for the various sensors, any deformation of this plate can corrupt the sensor measurement. Choosing the ground mounting locations to be as close as possible to the fixed ends of the beams addresses both these issues. When such an ideal ground mounting locations are not practically feasible, the ground compliance should be appropriately modeled in the prediction and design process.

3. The various "supposedly rigid" intermediate stages between ground and primary motion stage always have some finite compliance. This compliance can be reduced by appropriate choice of geometry and dimensions, but is difficult to eliminate. As shown in this paper, even when the secondary stage thickness was made more than 15 times the thickness of the beam flexures, the secondary stage compliance remains non-negligible. Furthermore, bulking up the stages also lowers natural frequencies, which can be detrimental to dynamic performance. Again, compliance of these various stages should be appropriately modeled in the prediction and design process.

4. There are unavoidable manufacturing tolerances that lead to imperfect flexure beam and overall mechanism geometry. In general, this adversely impacts bearing direction stiffness and error motions.

References

[1] Awtar S. Synthesis and Analysis of Parallel Kinematic XY Flexure Mechanisms, Sc.D Thesis. Cambridge MA: Massachusetts Institute of Technology; 2004.
[2] Brouwer DM. Design principles for six degrees-of-freedom MEMS-based precision manipulators. Netherlands: University of Twente; 2007.
[3] Smith ST. Flexure – Elements of Elastic Mechanisms. CRC Press; 2000.
[4] Legtenberg R, Groeneveld AW, Elwenspoek M. Comb drive actuators for large displacements. J Micromech Microeng 1996;6:320–9.
[5] Meijaard JP, Brouwer DM, Jonker JB. Analytical and experimental investigation of a parallel leaf spring guidance. Multibody Syst Dyn 2010;23:77–97.
[6] Brouwer DM, Meijaard JP, Jonker JB. Large deflection stiffness analysis of parallel prismatic leaf-spring flexures. Precis Eng 2013;37:505–21.
[7] Jones RV. Some uses of elasticity in instrument design. J Sci Instrum 1962;39:193–203.
[8] Awtar S, Slocum AH, Sevincer E. Characteristics of beam-based flexure modules. ASME J Mech Des 2006;129:625–39.
[9] Grade JD, Jerman H, Kenny TW. Design of large deflection electrostatic actuators. ASME/IEEE J Microelectromech Syst 2003;12:335–43.
[10] Olfatnia M, Sood S, Gorman J, Awtar S. Large stroke comb-drive actuators based on the clamped paired double parallelogram flexure. ASME/IEEE J Microelectromech Syst 2013;22:483–94.
[11] Hiemstra D. Design of Moving Magnet Actuators for Large-range Flexure-based Nanopositioning, M.S Thesis. Ann Arbor, MI: University of Michigan; 2014.
[12] Jerman, J.H., Grade, J.D., 2003, Miniature Device with Translatable Member, US Patent 6,664,707.
[13] Brouwer DM, Otten A, Engelen JBC, Krijnen B, Soemers HMJR. Long-range elastic guidance mechanisms for electrostatic comb-drive actuators. In: Proc. 10th International Conference of EUSPEN. 2010.
[14] Panas RM, Hopkins JB. Eliminating underconstraint in double parallelogram flexure mechanisms. ASME J Mech Des 2015;137:092301 (9 pages).
[15] Olfatnia M, Sood S, Awtar S. An asymmetric flexure mechanism design for electrostatic comb-Drive actuators. Rev Sci Instrum 2012;83:116105 (3 pages).
[16] Awtar S, Quint J. In-plane flexure based clamp. Precis Eng 2012;36:658–67.
[17] Awtar S, Slocum AH. Target block alignment error in XY stage metrology. Precis Eng 2007;31:185–7.